

# Structural evolution of nanoporous gold during thermal coarsening

Yu-chen Karen Chen-Wiegart<sup>a,\*</sup>, Steve Wang<sup>b</sup>, Yong S. Chu<sup>c</sup>, Wenjun Liu<sup>b</sup>,  
Ian McNulty<sup>b</sup>, Peter W. Voorhees<sup>a</sup>, David C. Dunand<sup>a</sup>

<sup>a</sup> Department of Materials Science and Engineering, Northwestern University, Evanston, IL 60208, USA

<sup>b</sup> Advanced Photon Source, Argonne National Laboratory, Argonne, IL 60439, USA

<sup>c</sup> National Synchrotron Light Source II, Brookhaven National Laboratory, Upton, NY 11973, USA

Received 26 January 2012; received in revised form 11 May 2012; accepted 12 May 2012

Available online 29 June 2012

## Abstract

The three-dimensional evolution of nanoligaments of nanoporous gold created by Ag–Au dealloying was studied during isothermal coarsening by X-ray nanotomography and microbeam Laue diffraction. The surface normal orientation, curvature and size of the gold nanoligaments were measured as a function of coarsening time (from 2 to 320 min). The following observations were made at 550, 600 and 650 °C. First, the distribution of orientations for the surfaces of the nanoligaments becomes more anisotropic with coarsening time, with an increasing area of the surfaces having a low surface energy, consistent with the growth of facets. Second, the curvature distribution of the nanoligaments (scaled by their size) also evolves during coarsening. The evolution of both surface orientation and scaled surface curvature indicates that coarsening does not occur in a self-similar manner, i.e. the interfacial shape distribution of the gold nanoligaments is not self-similar over time as they coarsen. This is consistent with the ligament size not being described by a classical temporal power law for coarsening systems. All three effects, and in particular the increased prevalence of surfaces with a low surface energy at long coarsening times, may affect the surface functionalities and properties of nanoporous gold in various applications, e.g. as catalysts, sensors and actuators.

© 2012 Acta Materialia Inc. Published by Elsevier Ltd. All rights reserved.

**Keywords:** Metal foam; Isothermal heat treatments; X-ray computed tomography; Transmission X-ray microscopy; Three-dimensional characterization

## 1. Introduction

Nanoporous metallic materials with open porosity have attracted attention due to their potential applications in various fields, e.g. as sensors [1,2], actuators [3], catalysts [4,5], battery electrodes [6], fuel cells [7], and super-capacitors [8]. One of the most effective ways of fabricating open nanopores in a metal is by dealloying: upon selective etching of the less noble element in a binary alloy the more noble element forms a sponge-like, porous structure with a bi-continuous

structure of pores and metal ligaments with sizes of 3–20 nm [9–12].

The metal nanoligaments (and thus the surrounding nanopores) can be coarsened by thermal annealing up to the micrometer scale [13–15]. Understanding this thermal coarsening process is essential for the application of nanoporous metals, since the pore and ligament sizes determine the mechanical, chemical and optical properties of nanoporous metals [16,17]. Furthermore, the shape and orientation of the nanoligament surface (i.e. the interface between the ligament and the pores) can also change during thermal coarsening.

As the dealloying front propagates through the alloy coarsening of the dealloyed layers takes place in the electrolyte, and atomic modeling has been carried out to understand this concurrent coarsening and the resulting nanoporous (np-)Au morphology [18]. In contrast, the emphasis of the

\* Corresponding author. Present address: Building 725D, 75 Brookhaven Avenue, Upton, NY 11973, USA. Tel.: +1 631 344 3563; fax: +1 631 344 3238.

E-mail address: [ycchen@bnl.gov](mailto:ycchen@bnl.gov) (Y.-c.K. Chen-Wiegart).

<sup>1</sup> Yu-chen Karen Chen-Wiegart was published under Yu-chen Karen Chen.

present paper is on the post-dealloying coarsening occurring during thermal annealing, as recent literature has addressed the importance of thermal coarsening in np-Au. Using scanning electron microscopy (SEM) Kertis et al. qualitatively showed that self-similarity exists between the subsequent coarsened morphologies and how the crystallographic structure of the grains are manifest in the porous structure [13]. Also, partial sintering has been observed on the surface of a np-Au thin film coarsened at 200–400 °C for 10 min, but the underlying mechanism remains unclear [15]. Li and Sieradzki observed a ductile to brittle mechanical property transition by conducting three point bending experiments to study the fracture behavior of np-Au samples annealed at 100–800 °C for 10 min. Samples annealed above 300 °C for 10 min were found to develop ductile properties [19]. This type of annealed sample is mechanically more stable and may be used in a wider range of applications. Various others have studied the yield strength of np-Au samples coarsened up to 600 °C and demonstrated that, at the nanometer length scale, the strength of a porous structure is governed by its ligament size, in addition to relative density [14,16,20,21]. The annealing atmosphere (i.e. helium vs. ozone) was also found to have an impact on the coarsening rate, which was explained by a change in surface chemistry [22]. However, many questions concerning the thermal coarsening of np-Au remain unexplored, as described below.

First, evolution of the size of np-Au the filament as a function of the coarsening time and temperature, which is controlled by the coarsening mechanism, has not to date been systematically quantified in a three-dimensional (3-D) manner. Fourier analysis has been used to quantify the characteristic length scale in thin films of np-Au [23]. The authors found that in SEM and transmission electron microscopy (TEM) images of np-Au a significant peak in the power spectrum exists, reflecting the characteristic length scale of the quasi-periodic structure. However, this method is difficult to apply to bulk samples.

Second, no experimental observations exist addressing whether the shape of the ligament/pore interface of np-Au is self-similar during coarsening. Erlebacher, in recent kinetic Monte Carlo simulations, concluded that the coarsening of np-Au is controlled by a surface diffusion controlled Rayleigh instability, which naturally results from pinch-off events [24]. Due to the same time dependence for pinch-off events and surface flattening, the simulations showed that thermal coarsening of np-Au does not preserve the interfacial shape of the pore/gold interface during thermal coarsening. Evolution of the shape of the interface is thus not self-similar over time (referred as “non self-similar” below). Experimentally, researchers have imaged as-dealloyed np-Au from TEM tomographic reconstructions and measured the ligament curvature distribution [25,26]. Serial sectioning and reconstruction using focused ion beam methods have been used to reconstruct the 3-D structure of one as-dealloyed np-Au sample, but structure evolution during thermal coarsening was not investigated [27]. Because it is a destructive method it cannot be used

to continuously study the structure evolution of a single sample. In previous work using X-ray nanotomography we presented a quantitative morphological and topological analysis of a single np-Au sample coarsened at 400 °C for 30 min [28].

Third, the evolution of the morphological anisotropy of the np-Au structure as a function of coarsening time and temperature is unknown. We previously reported the presence of a slight crystallographic anisotropy in the np-Au sample annealed at 400 °C for 30 min [28] and hypothesized that it is due to the dominance of surfaces with low surface energy crystallographic planes. While Hakamada et al. have shown a crystallographic preferred orientation of {111} using a Schulz diffraction method in np-Au during thermal coarsening [29] and Kertis et al. have observed faceting of gold ligaments in coarsened nanoporous gold [13], the correlation between the morphology and crystallographic orientation of np-Au is still unclear.

In this paper we present a quantitative study of isothermal coarsening (referred to as “coarsening” below) in np-Au to address the above questions, i.e. the dependence of ligament size and curvature, as well as the spatial and crystallographic orientations, upon annealing time and temperature. X-ray nanotomography using a transmission X-ray microscope was used to follow the coarsening behavior ex situ for the same specimen at various temperatures. This technique is especially well suited to the study of coarsening in nanoporous metals compared with other 3-D imaging characterization techniques [30], given that it has a relatively high resolution (~30 nm) [31–33], excellent penetration in high Z Au samples (tens of microns in thickness, allowing a bulk study) and is non-destructive (allowing the study of the evolution of a single sample). We also characterized the crystallographic orientation of the nanoporous gold samples by microbeam Laue diffraction. The coarsening mechanism and the microstructural evolution are discussed.

## 2. Experimental procedures

### 2.1. Sample preparation

Cylindrical np-Au samples were created for this work. First, an Ag–30 at.% Au alloy was arc melted from the pure elements (99.99% pure, Kurt J. Lesker). Wires of this alloy were then created by the Taylor method [34,35] in Pyrex glass tubes, with a diameter of 20–50 μm. The tube was fractured and the tip of the fine wire protruding from the Pyrex sheath was then further shaped by focused ion beam (FIB) milling into a cylindrical pillar ~30 μm high and ~16 μm in diameter. The FIB shaped tip was submerged in a concentrated nitric acid bath (11.7 M, 75 vol.% commercial nitric acid, 68–70% assay, in deionized water) for 16 h to achieve complete dealloying. The tip was then mechanically clamped in a drill chuck and mounted on a customized stainless steel sample holder with a kinematic mount, which is compatible with both

transmission X-ray microscopy (TXM) and high temperature exposure. The kinematic mount allows a positioning reproducibility of  $\sim 1\text{--}2\ \mu\text{m}$  between annealing steps in all three directions.

## 2.2. X-ray nanotomography

Four dealloyed samples were annealed in laboratory air at 550, 600, 650, and 800 °C. Only the 800 °C annealed sample was not pre-shaped by FIB before dealloying. To observe the continuous morphological evolution the tomographic studies of nanoporous gold coarsening were conducted *ex situ*. Annealing was performed by placing the sample in a box furnace preheated to the desired temperature and annealing it in air. The sample was then removed from the furnace and air cooled, followed by TXM tomographic measurement. The above procedure was then repeated on the same sample for increased annealing times. While the annealing time ranged from 5 min to  $> 5\ \text{h}$ , for a  $20\ \mu\text{m}$  cylindrical np-Au sample with a high surface to volume ratio the heating rate in a convection box furnace with a large thermal mass and the air cooling rate of the samples are fast enough that any effect of the heating and cooling rates is negligible. We used the TXM instrument in the 32-ID-C beamline at the Advanced Photon Source (Argonne National Laboratory, Argonne, IL) [28,33]. This microscope uses a Fresnel zone plate as the objective lens with a resolution of about 30 nm in two dimensions [32,36]. 361 projections were recorded for each annealing step with a 10.4 keV beam over a  $180^\circ$  range (one image every  $0.5^\circ$ , with an exposure time of 2 s) with a lens-coupled CCD detector with a resolution of  $2048 \times 2048$  pixels.

The 3-D structures were reconstructed from these projections using a standard filtered back-projection algorithm [37]. Smoothing and segmentation algorithms were applied to the reconstructed images [38]. Standard 3-D Gaussian smoothing was performed to reduce the level of noise: a 3-D Gaussian function with variance  $\sigma^2 = 1.44\ \text{pixel}^2$  was convolved with the data pixel by pixel [38]. Segmentation, including thresholding and eliminating “free floating” particles within the structure, was then applied to the smoothed images. A 3-D mesh approximation (of triangular shape) of the surface was then generated using a standard built-in function of the IDL programming language (IDL 7.0, ITT Visual Information Solutions Ltd) on which to perform further analysis. Interfacial shape distributions (ISDs), which display the probability of finding a patch of interface with a given pair of principle curvatures, were used to analyze the pore curvature and thus quantify the ligament shape evolution. Thus the distribution represents the global shape of the interface. ISDs have been used to quantify other structures in three dimensions, including dendrites and bi-continuous structures, such as np-Au [28,39–41]. For instance, the data in the first and third quadrants of an ISD (i.e. with principle curvatures of the same sign) indicate the existence of convex and concave points, respectively, in a

characterized structure, while those in the second quadrant indicate saddle points. The interfacial normal distributions (INDs) [42,43], in which the fraction of normals to surface patches pointing in a given direction is plotted in a stereographic projection along a chosen axis, were used to quantify the preferred orientation of the ligaments in space.

## 2.3. Micro-beam Laue diffraction experiments

Micro-beam Laue diffraction was performed in beamline 34-ID-E at the Advanced Photon Source to characterize the crystal orientation of two np-Au samples, after they had been imaged by TXM experiments following their final coarsening step at 600 and 650 °C (160 min).

A “pink” beam ( $\sim 7\text{--}30\ \text{keV}$ ), focused by a set of Kirkpatrick–Baez focusing mirrors, with a beam cross-section of  $0.3 \times 0.5\ \mu\text{m}$  was used [44,45]. A Perkin Elmer amorphous silicon area detector was used with a 1 s exposure time. Laue diffraction patterns were collected for a  $20 \times 20\ \mu\text{m}$  area of the tip of the sample (including the TXM imaging area), which was scanned by the X-ray beam with a step size of  $1\ \mu\text{m}$  in both the vertical and horizontal directions. All the collected patterns were then indexed to determine the crystallographic orientation at each scanned point, and superimposed into pole figures.

Furthermore, an as-cast Ag–Au alloy wire was characterized by scanning the sample vertically and horizontally. The horizontal scan was across the  $20\text{--}50\ \mu\text{m}$  diameter of the wire with a  $5\ \mu\text{m}$  step size. The vertical scan distance was  $\sim 200\ \mu\text{m}$  with a  $5\ \mu\text{m}$  step size.

## 3. Results

### 3.1. Evolution of ligament morphology and volume fraction

Fig. 1 shows a series of TXM projections, at the same angle, for np-Au coarsened at 650 °C for various times. The porous structures of np-Au can be clearly seen by TXM, even at very short coarsening times (5 min) and for small features (size of pores and ligaments  $< 100\ \text{nm}$ ). Both the pores and the gold ligaments coarsened as a function of annealing time. No significant densification, which would lead to changes in porosity and sample shape, was observed in the projections as the overall shape of the sample tip remained approximately the same. Circular artifacts seen in the projections are due to imperfections in the condenser [46] of the transmission X-ray microscope. Therefore, during analysis we used the central volume ( $\sim 5\ \mu\text{m}$  from the tip of the sample and  $\sim 2\ \mu\text{m}$  from the cylinder surface of the sample) to avoid the effects of these artifacts.

Fig. 2 shows a series of 3-D reconstructions of the same np-Au central volume (as mentioned above), representative of the bulk, for the sample annealed at 650 °C for 5–160 min. Each data set with a volume of  $200 \times 200 \times 200$  pixels (corresponding to  $\sim 6.5 \times 6.5 \times 6.5\ \mu\text{m}$ , given a voxel size of  $32 \times 32 \times 32\ \text{nm}$ ) was segmented. The reconstructions revealed a continuous coarsening of both the

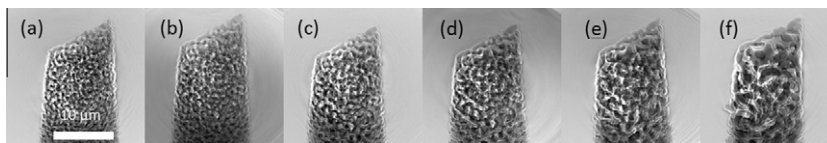


Fig. 1. TXM micrograph projections of a nanoporous gold tip coarsened at 650 °C for (a) 5 min, (b) 10 min, (c) 20 min, (d) 40 min, (e) 80 min and (f) 160 min.

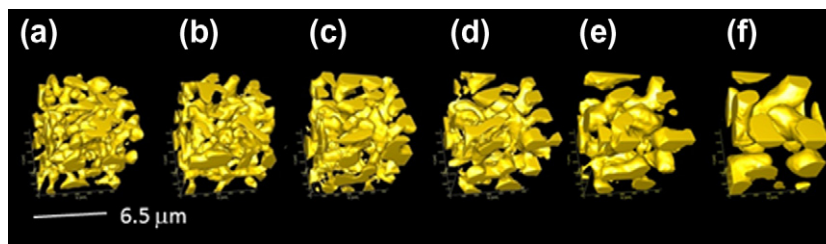


Fig. 2. 3-D reconstruction of the nanoporous gold bulk region after coarsening at 650 °C for (a) 5 min, (b) 10 min, (c) 20 min, (d) 40, (e) 80 min and (f) 160 min.

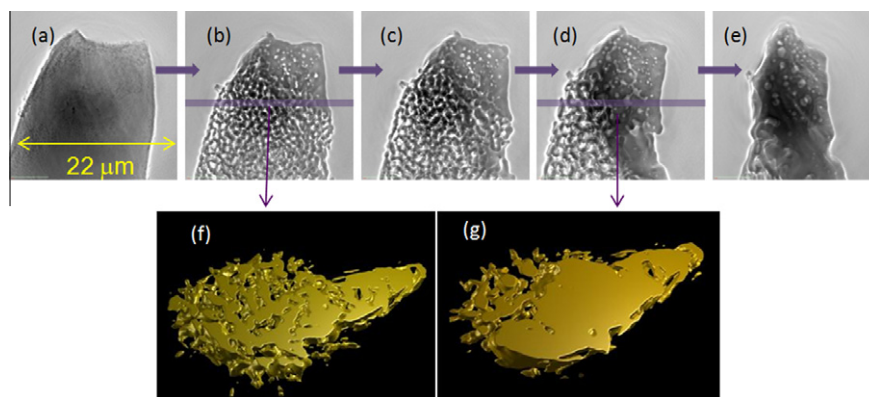


Fig. 3. TXM micrograph projections of nanoporous gold coarsened at 800 °C for (a) 0 min, (b) 2 min, (c) 4 min, (d) 8 min, and (e) 32 min. Reconstructed cross-sections after (f) 2 min and (g) 8 min. The locations of these cross-sections are shown in (b) and (d), respectively.

pores and gold ligaments in three dimensions with no apparent densification. The ligaments and the pores are both interconnected, forming a bi-continuous structure [23]. The ligaments and pores together are referred to as “features” as they coarsen in the remainder of this article. The architecture remains bi-continuous throughout the coarsening process. A qualitative ISD analysis, discussed in a later section, addresses whether the features coarsen in a self-similar or shape-preserved manner [24], i.e. whether the morphologies of the feature at consecutive coarsening times are only scaled with the feature size.

Fig. 3a–e shows TXM micrograph projections of the np-Au sample coarsened at 800 °C for 2–32 min. It is apparent that, unlike the samples coarsened at lower temperatures, sintering took place. This was confirmed by reconstructed cross-sections after 2 and 8 min (Fig. 3f and g), which show a clear reduction in porosity. Sintering is more pronounced at the narrower end of the irregularly shaped tip after 2 min sintering (Fig. 3f), where the coarsened pores reached a size comparable with the local sample size. Sintering progressed

over the majority of the cross-section after 8 min (Fig. 3g). The projection after 32 min (Fig. 3e) shows that the tip was nearly fully densified and had very significantly changed its shape.

The TXM projections and reconstructions of np-Au samples coarsened at 550 and 600 °C reveal the same coarsening behavior as the np-Au sample coarsened at 650 °C, as presented in Figs. 1 and 2: a continuous coarsening behavior was observed in the bi-continuous structures without measurable densification. Fig. 4 shows the Au volume fraction in the nanoporous samples coarsened at 550, 600, and 650 °C, from 10 min to ~6 h. While a slight trend towards a higher fraction (i.e. densification) with increasing time might be present, the volume fraction can be considered to remain constant at ~28% (the average is 28.4% with a standard deviation of 2.1%), indicating that sintering is negligible in this region of the sample, which is expected to be representative of the bulk behavior. For this reason in the remainder of this paper the coarsening of these three samples (coarsened at 550, 600 and 650 °C) is presented

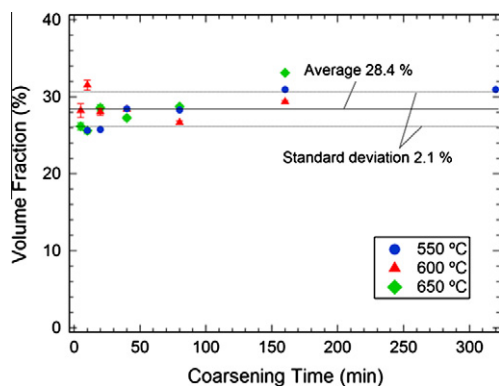


Fig. 4. Plot of gold volume fraction in the nanoporous gold sample vs. coarsening time at 550, 600 and 650 °C.

with detailed quantitative analyses, while the sample coarsened at 800 °C, which showed extensive sintering (Fig. 3), is not further discussed.

### 3.2. Evolution of feature size

Nanoporous gold exhibits a complex sponge-like network with ligament cross-sections that vary continuously between nodes, so an average ligament diameter is unrepresentative. Rather, here we use the inverse of the specific area, where the specific area ( $S_A$ ) is calculated as the ratio of solid (gold) surface to solid volume, and we take  $1/S_A$  to represent the feature size, as was done by Kwon et al. [41]. Fig. 5 displays a plot of inverse specific area (feature size) vs. coarsening time, showing that coarsening occurs at a rate that increases with temperature. At coarsening time  $t = 0$  the inverse specific area, taken to be  $20 \pm 10$  nm, is below the resolution of TXM and therefore was estimated from our other diffraction-based X-ray imaging work [47] and the literature [25,26]. Notice that rapid coarsening took place during the first 5–10 min.

### 3.3. Evolution of interfacial shape distributions

ISD evolution was examined as a function of coarsening time at 550–650 °C (Supplementary Figs. 1–3). However,

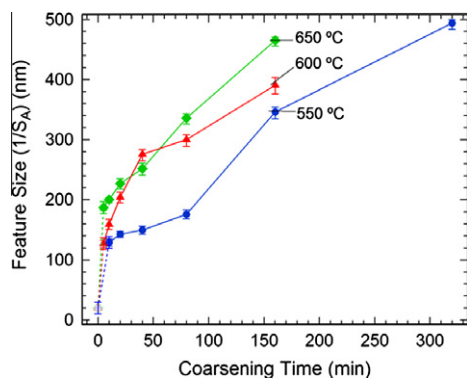


Fig. 5. Plot of feature size (inverse specific area  $1/S_A$ ) vs. coarsening time at 550, 600 and 650 °C. The point  $t = 0$  ( $1/S_A = 20 \pm 10$  nm) is from the literature.

since the feature size increases with increasing coarsening time it is difficult to compare the shape of the pore/ligament interface at different coarsening times, thus a series of ISD plots in which the curvatures are scaled with the feature size ( $1/S_A$ ) at 650 °C are shown in Fig. 6.

First, it is apparent that the distribution mostly falls within the second quadrant of the ISD, which corresponds to saddle-shaped surfaces where the principal curvatures  $\kappa_1$  and  $\kappa_2$  have opposite signs. The area integral of the total probability has been normalized to unity. A smaller part of the distribution also falls within the first quadrant ( $\kappa_1$  and  $\kappa_2$  positive), indicating the presence of convex shapes among the gold ligaments. Only a few concave points (<1%, third quadrant) were observed on the gold ligaments.

Despite this normalization, in Fig. 6a–f a broadening of the ISD is observed with increasing aging time, indicating that the curvature decreases more slowly than the rate at which the length scale  $S_A^{-1}$  grows. This is a clear indication that the interfacial shape changes during coarsening, i.e. it is not self-similar over time. The same behavior was also observed for coarsening at 550 and 600 °C (see Supplementary Figs. 4 and 5).

### 3.4. Evolution of interface normal distributions

As shown in the previous section, the interfacial shape changes during coarsening, meaning that the coarsening of np-Au is not self-similar, i.e. the initial structure of the surface does not differ from that at later times by simple magnification of the earlier structure. This implies that processes involving more than a simple change in length scale of the structure must be occurring during coarsening. To further assess this phenomenon the evolution of the spatial orientation of the gold/pore interface was examined. Here we discuss how the ligament–pore interfaces are oriented with respect to the sample coordinate system. The crystallographic orientation of these surfaces will be addressed in the following section. The spatial orientation of the ligament–pore interface can be quantitatively determined using interfacial normal distributions (INDs), which were calculated by the following steps [42]. First, the normal direction for each individual surface patch was calculated among the surface. These normal directions are then stereographically projected along the laboratory  $x$ -direction: this is an arbitrary direction perpendicular to the wire axis (longitudinal direction along the wire) which corresponds to the beam direction when the sample stage is at  $0^\circ$ ). An inhomogeneous distribution in the resulting IND indicates anisotropy of the interfacial morphology [42]. This is visible in Fig. 7a–f, which displays the INDs as a function of coarsening time at 650 °C. The maximum intensity of the INDs (representing the highest probability of a particular orientation) increases while the fraction of the plot in which there are no patches of a given orientation (colored a dark purple in Fig. 8a–f) also increases in area, thus the morphology of the np-Au features becomes more anisotropic

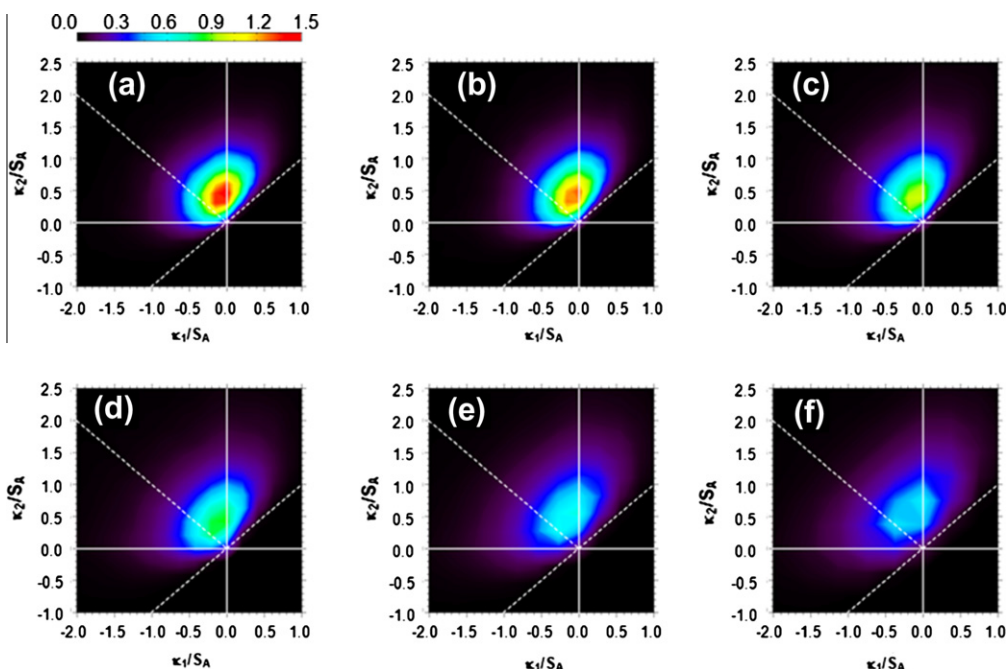


Fig. 6. Scaled interfacial shape distributions after coarsening at 650 °C for (a) 5 min, (b) 10 min, (c) 20 min, (d) 40 min, (e) 80 min and (f) 160 min.

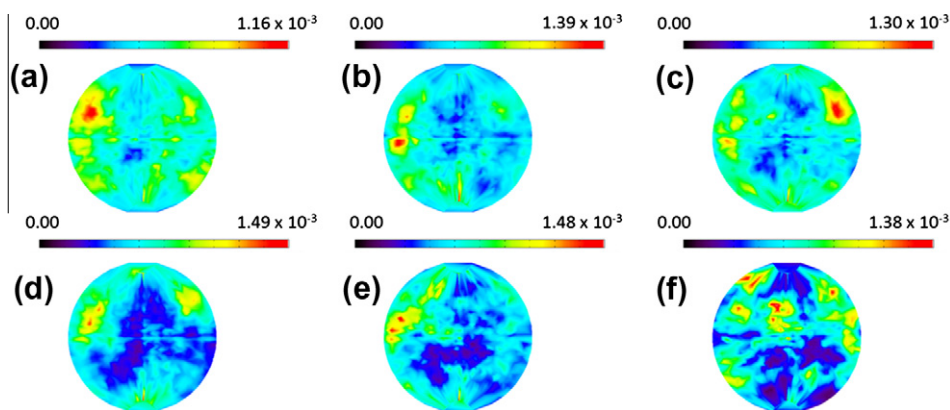


Fig. 7. The IND at 650 °C after coarsening for (a) 5 min, (b) 10 min, (c) 20 min, (d) 40 min, (e) 80 min and (f) 160 min.

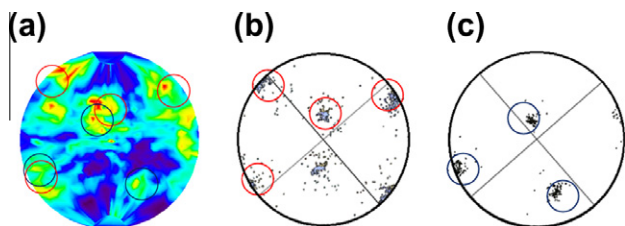


Fig. 8. Comparison of (a) the IND and (b) the  $\{111\}$  pole figure and (c) the  $\{001\}$  pole figure for a sample coarsened at 650 °C for 160 min. The red circles indicate matches between the peaks in the IND and the  $\{111\}$  pole figure. The blue circles indicate matches between the peaks in the IND and the  $\{001\}$  pole figure. (For interpretation of the references to colour in this figure legend, the reader is referred to the web version of this article.)

as coarsening proceeds. The same behavior was also observed for coarsening at 550 and 600 °C (see Supplementary Figs. 7 and 8).

### 3.5. Micro-beam Laue diffraction of coarsened $np$ -Au samples

All diffraction patterns from the as-cast wire were the same, indicating that the as-cast wires are single crystals within the region scanned (20–50  $\mu\text{m}$  in diameter and  $\sim 200$   $\mu\text{m}$  in length) or, more likely, show very coarse bamboo grains.

The Laue diffraction patterns were collected during scanning with the X-ray microbeam. The crystallographic orientation of each individual scanned position was then analyzed and collected into pole figures. The pole figures for the tips coarsened for 160 min at 600 and 650 °C are presented in Figs. 8 and 9, respectively, and show distinctive peaks, as expected for a single crystal with some misorientation, e.g. due to the presence of sub-grains. To determine the relationship between the spatial orientation

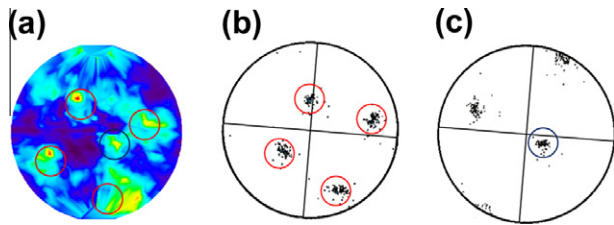


Fig. 9. Comparison of (a) the IND and (b) the  $\{111\}$  pole figure and (c) the  $\{001\}$  pole figure for a sample coarsened at 600 °C for 160 min. The red circles indicate matches between the peaks in the IND and the  $\{111\}$  pole figure. The blue circle indicates matches between the peaks in the IND and the  $\{001\}$  pole figure. (For interpretation of the references to colour in this figure legend, the reader is referred to the web version of this article.)

of the ligament–pore interfaces and the crystallographic orientation of the np-Au sample these pole figures were directly compared with the IND plots. The strongest IND peaks match the  $\{111\}$  normal orientation (marked as red circles in Figs. 8 and 9) and a few weaker peaks also match  $\{100\}$  marked as blue circles in Figs. 8 and 9).

## 4. Discussion

### 4.1. Evolution of ligament size and shape

As shown in Fig. 3, on coarsening at 800 °C the tip changed shape very significantly as it was sintered. This indicates that at this stage of coarsening the length scale of the ligaments and pores approaches the sample size.

For a coarsening process without densification it is well-known that  $d \propto t^{1/n}$ , where  $d$  is the feature size,  $t$  is the coarsening time and  $n$  correlates with the mechanism controlling coarsening [11]. A value of  $n=3$  indicates that bulk diffusion is controlling the process, while  $n=4$  shows that surface diffusion dominates. The literature on solid-state coarsening has widely adopted double logarithmic plots of  $d$  vs.  $t$  as the method to determine the value of  $n$  from the slope of the best fit curve [11,48]. However, this requires that  $d$  at the beginning of self-similar coarsening is small compared with  $d$  at later times, which is not true for coarsening of np-Au, because a non-zero feature size exists before coarsening begins. Therefore plots of  $d^3$  vs.  $t$  and  $d^4$  vs.  $t$  were created (see Supplementary Fig. 6). The dominant coarsening mechanism can, in principle, be determined by comparing the best linear fit to these two plots. However, all fittings result in similar coefficients of determination ranging from  $R^2 = 0.92$  to 0.98. A reasonable explanation for the inability to determine an exponent is that the structure is coarsening in a non-self-similar manner and thus the standard power law description of the average length scale in the system would not be expected to hold. An example of such coarsening is coarsening of the dendrite structure in semi-solid Pb–Sn alloys [42]. Independent of the time exponent, however, assuming that the initial structure is similar at each temperature gives

information about the dominant coarsening mechanism by plotting the feature size  $d$  against the product  $kt$ , with  $t$  the coarsening time and  $k = \exp(-Q/RT)$ , where  $Q$  is the activation energy for the coarsening mechanism,  $R$  is the Boltzmann constant and  $T$  is the coarsening temperature. With an accurate choice of  $Q$  the data acquired at different temperatures  $T$ , provided np-Au coarsening follows the same mechanism, should superimpose in the plot. As shown in Fig. 10a and b, the  $d$  vs.  $kt$  plots show a much better data overlay with  $Q = Q_s = 62 \text{ kJ mole}^{-1}$ , the surface diffusion activation energy of gold, than with  $Q = Q_v = 212 \text{ kJ mole}^{-1}$ , the volume diffusion activation energy of gold. This is a strong indication that the coarsening of np-Au is a result of surface diffusion, as also suggested by Erlebacher [24] using kinetic Monte Carlo simulations.

If the system was in a non-self-similar coarsening regime then the scaled ISDs shown in Fig. 6 should not be time-invariant, as is the case. Thus from both measurement of the average length scale and the ISDs we conclude that the np-Au structures are not coarsening in a self-similar fashion. The reason for the non-self-similarity may be the increasing anisotropy of the structure as a function of coarsening time (see below).

Although it was pointed out by Kertis et al. [13] that np-Au appears to coarsen in a self-similar manner by qualitative observation of SEM images, our quantitative analysis of the 3-D np-Au structure shows that np-Au does not preserve a constant interfacial shape during coarsening. This is consistent with Erlebacher's Monte Carlo simulations, in which he showed that, due to time-dependent pinch-off events, thermal coarsening does not preserve the shape of the np-Au interface [24].

The scaled ISDs are not symmetrical about the zero mean curvature line (dotted line in Fig. 6, where  $\kappa_2 = -\kappa_1$ ). This is because as the solid volume fraction departs from 50% the average mean curvature deviates from zero. The gold volume fraction shown here,  $28.4 \pm 2.1\%$ , differs from our previous result [27], where dealloying a Ag–30Au alloy resulted in a nanoporous gold structure with a gold volume fraction of  $50 \pm 5\%$  and therefore an ISD symmetrical about the zero mean curvature line. While sample and location variation could be the reason for the difference in gold volume fraction, this may also be caused by errors in image segmentation in the previous result. The feature size was much finer in the previous result due to the lower annealing temperature (400 °C) and the shorter annealing time (10 min). In addition, the internal feature edges of the sample were purposely enhanced using Zernike phase contrast. As a result, the morphology can be identified, but it is difficult to segment using a simple thresholding method. Nevertheless, the shape of the ISD and anisotropy in the INDs remain similar. The quality of the data used in the quantitative analysis is here much improved and the features can be well resolved as the samples were coarsened at a higher temperature (above 550 °C) and for a longer time (5–160 or 320 min).

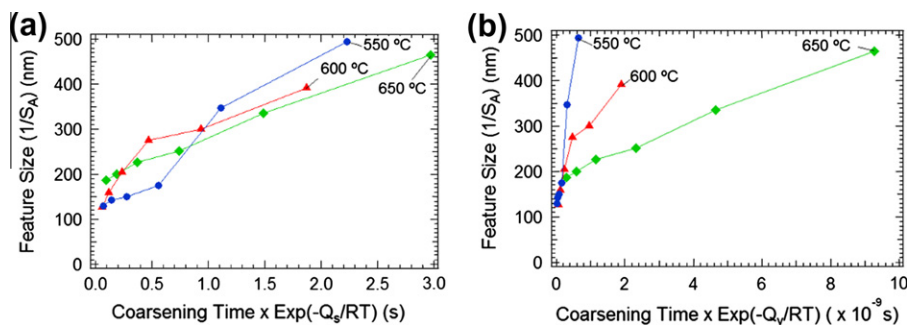


Fig. 10. Plot of feature size (inverse specific area  $1/S_A$ ) vs. coarsening time  $\times \exp(-Q/RT)$ . (a)  $Q = Q_s$  is the gold surface diffusion activation energy,  $Q_s = 62 \text{ kJ mole}^{-1}$  [55]. (b)  $Q = Q_v$  is the gold bulk diffusion activation energy,  $Q_v = 212 \text{ kJ mole}^{-1}$  [56].

#### 4.2. Interface normal distributions and Laue microdiffraction

In addition to changes in interfacial shape, an increase in anisotropy with coarsening time is visible in the INDs shown in Fig. 9. The origin of this anisotropy, which reflects a preferred spatial orientation of the ligament–pore interfaces, can be explained by correlating this spatial orientation with the crystallographic orientation of the pore–gold interface of np-Au.

We previously reported a slight anisotropy in np-Au annealed for 30 min at 400 °C, which we hypothesized was due to np-Au surface planes with a low surface energy ( $\gamma$ ) being preferred compared with those with a higher surface energy when the structure is undergoing coarsening. For gold within the temperature range studied here (550–800 °C),  $\gamma\{111\} < \gamma\{100\} < \gamma\{110\}$ , and the ligament–pore interfaces are typically faceted, as observed by high resolution electron microscopy [49].

Direct comparison of the pole figures with the IND shows that the strongest IND peaks match some of the peaks in the  $\{111\}$  normal orientation (red circles in Figs. 8 and 9), the plane with the lowest surface energy. A few weaker peaks then match  $\{100\}$  blue circles in Figs. 8 and 9), the next lower index plane with the second lowest  $\gamma$  in gold. This correspondence between INDs and pole figures indicates that the preferred crystallographic orientations may result in a preferred interfacial surface spatial orientation during coarsening, indicating that the np-Au inner surface is faceted to reduce the surface energy, as observed in gold nanoparticles, whose equilibrium shape was found to be a modified truncated octahedron consisting of  $\{111\}$  and  $\{100\}$  facets [50–52]. The fraction of surface area with a specific crystallographic orientation can be quantified by integrating the INDs at the positions corresponding to the specific crystallographic orientation. For the sample coarsened at 650 °C for 160 min the fraction of the total surface area which has a  $\{111\}$  orientation is 16.0% with a 10° angular tolerance and 4.2% with a 5° tolerance. The fraction of  $\{100\}$  orientation surfaces was 9.7% with a 10° angular tolerance and 2.6% for a 5° tolerance. The sample coarsened at 600 °C for 160 min showed a similar result: 14.7% (10°) and 3.6% (5°) for  $\{111\}$  and

$\{100\}$  (10°) and 2.1% (5°) for  $\{100\}$ . This results in an approximate  $\{111\}$  facet area to  $\{100\}$  facet area ratio of  $\sim 1.7$ , which may be useful for catalytic applications of np-Au, as the activity of the catalytic materials frequently corresponds to specific crystallographic orientations [5].

Although a crystallographic preferred orientation of  $\{111\}$  and faceting of gold ligaments on the surface in np-Au during thermal coarsening have been previously reported using SEM [13] and Schulz diffraction [29], here we have shown a correlation between the morphology (spatial orientation of the interface) and crystallographic orientation of np-Au. The appearance of facets is also consistent with the foam coarsening in a non-self-similar manner and the failure to find a relationship between  $1/S_A$  and the coarsening time with a fixed power law exponent. This is because the fraction of interface with a given facet orientation changes during the coarsening process.

This development of preferred orientations during coarsening of np-Au might be a general feature of other bi-continuous structures with anisotropic surface energies subjected to coarsening. Then annealing can be used as a tool not only to tune the feature size, but also to develop particular crystallographic orientations of the np-Au inner surface. These faceted surfaces may directly determine the function and properties of this material in various applications, such as catalysis [4], sensors [1] and actuators [3]. Thus future studies addressing feature size-dependent properties (e.g. optical and mechanical properties) resulting from annealing should also take into account evolution of the crystallographic orientation and faceting occurring during coarsening.

Further factors affecting coarsening of np-Au are residual silver atoms, partial oxidation of gold atoms during the dealloying process [53], and the presence of absorbed species, such as oxygen [54]. These additional species may play a role in affecting the coarsening behavior by modifying the surface diffusivity of gold atoms. For instance, the oxides of gold may increase the surface diffusivity [53] and the absorbed species could change the stress state on the surface [54]. The effects of these surface modifiers is beyond the scope of this paper and is left to future research.

## 5. Conclusions

The coarsening of np-Au, created by Ag–Au dealloying, was studied by X-ray nanotomography as a function of annealing time (from 2 to 320 min) and annealing temperature (550, 600, 650 and 800 °C). At 800 °C the np-Au sample was strongly sintered within 2 min, whereas at 550–650 °C coarsening without significant sintering was observed up to 320 min annealing time. For these latter samples 3-D tomographic reconstruction and segmentation were used to quantify the feature (ligament and pore) sizes, interfacial curvature and surface normal orientation. The following conclusions can be drawn.

The feature size (determined as the inverse of the specific area  $S_A^{-1}$ ) increases as a function of coarsening time, but does not exactly follow a power law over the timescales and length scales accessed in our experiments, so it cannot be determined whether bulk or surface diffusion controls coarsening. Consistent with this, we find that the interfacial morphology, as quantified by the interfacial shape distribution, is not self-similar over time. We find that the morphology of the structure becomes increasingly anisotropic with coarsening time, with the area of the interface with surfaces having a low interfacial energy increasing with time. This may be the cause of the non self-similar coarsening behavior. This implies that coarsening can be used as a mechanism to tune the properties of the nanoporous structures through this change in distribution of crystallographic orientations of the surfaces, thereby affecting the surface functionalities of nanoporous gold in various applications, e.g. as catalysts, sensors and actuators.

## Acknowledgements

We thank Dr R. Harder and Mr A. Deriy (both Argonne National Laboratory) for their assistance with the experimental TXM set-up and Ms A. Deymier and Ms A. Singhal (both Northwestern University) for their help with the TXM measurements. We also thank Dr Q. Shen (Brookhaven National Laboratory) for initial guidance with this project and Prof. Y. Hwu of the Academia Sinica for making the TXM instrument available at the Advanced Photon Source. We thank the referee for the suggestion in determining the coarsening mechanism. Use of the Advanced Photon Source is supported by the US Department of Energy, Office of Science, Office of Basic Energy Sciences, under contract no. DE-AC02-06CH11357. Y.K.C.-W. and Y.C. acknowledge support by the Brookhaven Science Associates, LLC under contract no. DE-AC02-98CH10886.

## Appendix A. Supplementary material

Supplementary data associated with this article can be found, in the online version, at <http://dx.doi.org/10.1016/j.actamat.2012.05.012>.

## References

- [1] Qiu HJ, Xue LY, Ji GL, Zhou GP, Huang XR, Qu YB, et al. *Biosens Bioelectron* 2009;24:3014–8.
- [2] Ding DY, Chen Z. *Adv Mater* 2007;19:1996.
- [3] Biener J, Wittstock A, Zepeda-Ruiz LA, Biener MM, Zielasek V, Kramer D, et al. *Nat Mater* 2009;8:47–51.
- [4] Xu C, Xu X, Su J, Ding Y. *J Catal* 2007;252:243–8.
- [5] Wittstock A, Zielasek V, Biener J, Friend CM, Baumer M. *Science* 2010;327:319–22.
- [6] Yu Y, Gu L, Lang XY, Zhu CB, Fujita T, Chen MW, et al. *Adv Mater* 2011;23:2443.
- [7] Snyder J, Fujita T, Chen MW, Erlebacher J. *Nat Mater* 2010;9:904–7.
- [8] Lang X, Hirata A, Fujita T, Chen M. *Nat Nanotechnol* 2011;6:232–6.
- [9] Weissmuller J, Newman R, Jin H, Hodge A, Kysar J. *MRS Bull* 2009;34:10.
- [10] Ding Y, Kim YJ, Erlebacher J. *Adv Mater* 2004;16:1897.
- [11] Qian LH, Chen MW. *Appl Phys Lett* 2007;91:083105-1–3.
- [12] Tappan BC, Steiner SA, Luther EP. *Angew Chem Int Ed* 2010;49:4544–65.
- [13] Kertis F, Snyder J, Govada L, Khurshid S, Chayen N, Erlebacher J. *JOM* 2010;62:50–6.
- [14] Cox ME, Dunand DC. *Mater Sci Eng A Struct Mater Propert Microstruct Process* 2011;528:2401–6.
- [15] Seker E, Gaskins JT, Bart-Smith H, Zhu J, Reed ML, Zangari G, et al. *Acta Mater* 2007;55:4593–602.
- [16] Hodge AM, Biener J, Hayes JR, Bythrow PM, Volkert CA, Hamza AV. *Acta Mater* 2007;55:1343–9.
- [17] Kucheyev SO, Hayes JR, Biener J, Huser T, Talley CE, Hamza AV. *Appl Phys Lett* 2006;89:3.
- [18] Kolluri K, Demkowicz MJ. *Acta Mater* 2011;7645–53.
- [19] Li R, Sieradzki K. *Phys Rev Lett* 1992;68:1168–71.
- [20] Biener J, Hodge AM, Hamza AV, Hsiung LM, Satcher JH. *J Appl Phys* 2005;97:4.
- [21] Biener J, Hodge AM, Hayes JR, Volkert CA, Zepeda-Ruiz LA, Hamza AV, et al. *Nano Lett* 2006;6:2379–82.
- [22] Biener J, Wittstock A, Biener MM, Nowitzki T, Hamza AV, Baeumer M. *Langmuir* 2010;26:13736–40.
- [23] Fujita T, Chen MW. *Jpn J Appl Phys* 2008;47:1161–3.
- [24] Erlebacher J. *Phys Rev Lett* 2011;106:225504-1–4.
- [25] Fujita T, Qian L, Inoke K, Erlebacher J, Chen M. *Appl Phys Lett* 2008;92:251902-1–3.
- [26] Rosner H, Parida S, Kramer D, Volkert C, Weissmuller J. *Adv Eng Mater* 2007;9:535–41.
- [27] Volkert CA, Lilleodden ET, Kramer D, Weissmuller J. *Appl Phys Lett* 2006;89:061920-1–3.
- [28] Chen YCK, Chu YS, Yi J, McNulty I, Shen Q, Voorhees PW, et al. *Appl Phys Lett* 2010;96:043122-1–3.
- [29] Hakamada M, Mabuchi M. *Mater Lett* 2008;62:483–6.
- [30] Robertson IM, Schuh CA, Vetrano JS, Browning ND, Field DP, Jensen DJ, et al. *J Mater Res* 2011;26:1341–83.
- [31] Chen TY, Chen YT, Wang CL, Kempson IM, Lee WK, Chu YS, et al. *Opt Exp* 2011;19:19919–24.
- [32] Chen YT, Chen TY, Yi JM, Chu YS, Lee WK, Wang CL, et al. *Opt Lett* 2011;36:1269–71.
- [33] Chu YS, Yi JM, De Carlo F, Shen Q, Lee WK, Wu HJ, et al. *Appl Phys Lett* 2008;92:103119-1–3.
- [34] Donald IW, Metcalfe BL. *J Mater Sci* 1996;31:1139–49.
- [35] Donald IW. *J Mater Sci* 1987;22:2661–79.
- [36] Chen Y, Lo T, Chu Y, Yi J, Liu C, Wang J, et al. *Nanotechnology* 2008;19:395302-1–5.
- [37] Natterer F. *The mathematics of computerized tomography*. New York: Wiley; 1986. p. 102–18.
- [38] Rosenfeld A. *Digital picture processing*. 2nd ed. New York: Academic Press; 1982.
- [39] Alkemper J, Voorhees PW. *Acta Mater* 2001;49:897–902.
- [40] Kwon Y, Thornton K, Voorhees P. *Phys Rev E* 2007;75:021120-1–5.

- [41] Kwon Y, Thornton K, Voorhees PW. *EPL* 2009;86:46005-1–5.
- [42] Kammer D, Voorhees PW. *Acta Mater* 2006;54:1549–58.
- [43] Fife JL, Li JC, Dunand DC, Voorhees PW. *J Mater Res* 2009;24:117–24.
- [44] Liu WJ, Ice GE, Tischler JZ, Khounsary A, Liu C, Assoufid L, et al. *Rev Sci Instrum* 2005;76:113701-1–6.
- [45] Liu W, Zschack P, Tischler J, Ice G, Larson B. 10th Int Conf X-ray Microscopy 2011;1365:108–11.
- [46] Zeng XH, Duewer F, Feser M, Huang C, Lyon A, Tkachuk A, et al. *Appl Opt* 2008;47:2376–81.
- [47] Kim S, Chen YCK, Putkunz CT, Dunand DC, McNulty I. *AIP Conf Proc* 2011;1365:411–4.
- [48] Hardy SC, Voorhees PW. *Metall Trans A Phys Metall Mater Sci* 1988;19:2713–21.
- [49] Flueli M, Borel JP. *J Cryst Growth* 1988;91:67–70.
- [50] Shim JH, Lee BJ, Cho YW. *Surf Sci* 2002;512:262–8.
- [51] Barnard AS, Lin XM, Curtiss LA. *J Phys Chem B* 2005;109:24465–72.
- [52] Muller CM, Mornaghini FCF, Spolenak R. *Nanotechnology* 2008;19:12.
- [53] Durkin P, Forty AJ. *Philos Mag A* 1982;45:95–105.
- [54] Dotzler CJ, Ingham B, Illy BN, Wallwork K, Ryan MP, Toney MF. *Adv Funct Mater* 2011;21:3938–46.
- [55] Beszeda I, Szabo IA, Gontier-Moya EG. *Appl Phys A* 2004;A78:1079–84.
- [56] Brandes EA, Brook GB. *Smithells metals reference book*. 7th ed. Elsevier; 1998. p. 13–9.